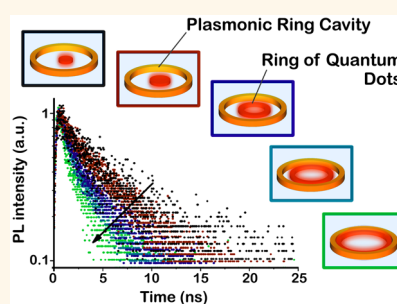# Plasmonic Control of Radiative Properties of Semiconductor Quantum Dots Coupled to Plasmonic Ring Cavities

Aliaksandra Rakovich,* Pablo Albella, and Stefan A. Maier

EXSS Group, Physics Department, Imperial College London, London, SW7 2AZ, U.K.

ABSTRACT In recent years, a lot of effort has been made to achieve controlled delivery of target particles to the hotspots of plasmonic nanoantennas, in order to probe and/or exploit the extremely large field enhancements produced by such structures. While in many cases such high fields are advantageous, there are instances where they should be avoided. In this work, we consider the implications of using the standard nanoantenna geometries when colloidal quantum dots are employed as target entities. We show that in this case, and for various reasons, dimer antennas are not the optimum choice. Plasmonic ring cavities are a better option despite low field enhancements, as they allow collective coupling of many quantum dots in a reproducible and predictable manner. In cases where larger field enhancements are required, or for larger quantum dots, nonconcentric ring-disk cavities can be employed instead.

When metal nanostructures are suitably designed, the excitation of localized plasmons yields strongly concentrated optical fields in their surroundings, often referred to as "hot spots". Such nanostructures can thus be considered to be effective optical antennas, able to convert propagating waves into localized fields.[1−3] This antenna function has ignited the development of a vast variety of applications, including surface-enhanced Raman scattering spectroscopy (SERS),[4−9] surface-enhanced infrared spectroscopy (SEIRS),[10−13] antenna-enhanced ultrafast nonlinear spectroscopy[14] and near-field microscopy[15,16] among others. A common requirement of most of these applications is the need to place a target entity in the vicinity of an antenna's hotspot to be able to exploit the enhanced fields and/or to enhance the target's functionality *via* interaction with the antenna. A lot of progress has been made recently to selectively deliver target entities to hotspots of dimer antennas,[17−19] since high field enhancements can be achieved in these configurations. In fact, the enhancement itself can be exploited in order to achieve selective localization of target entities.[20,21]

However, for practical purposes, one must consider the properties of these target entities when placed in the presence of high fields. In the case of fluorophores, for example, high excitation intensities are often detrimental to their efficiency and longevity (i.e., their photostability). In particular, at near single-emitter level, organic dyes photobleach quickly[22−25] and quantum dots (QDs) tend to blue-shift and also change their switching and radiative decay behavior after prolonged exposures to high intensities.[26−28] The small sizes of the hotspots of dimer nanoantennas limit the interaction to just a few emitters, effectively forcing the system toward such a single-emitter level. Furthermore, the small hotspot size is particularly detrimental when considering the large-area fabrication of plasmonics-based components for an all-optical on-chip circuitry aimed at optical data processing applications. This is because the process of distributing an equal number of fluorophores across a large area is often very difficult to achieve.
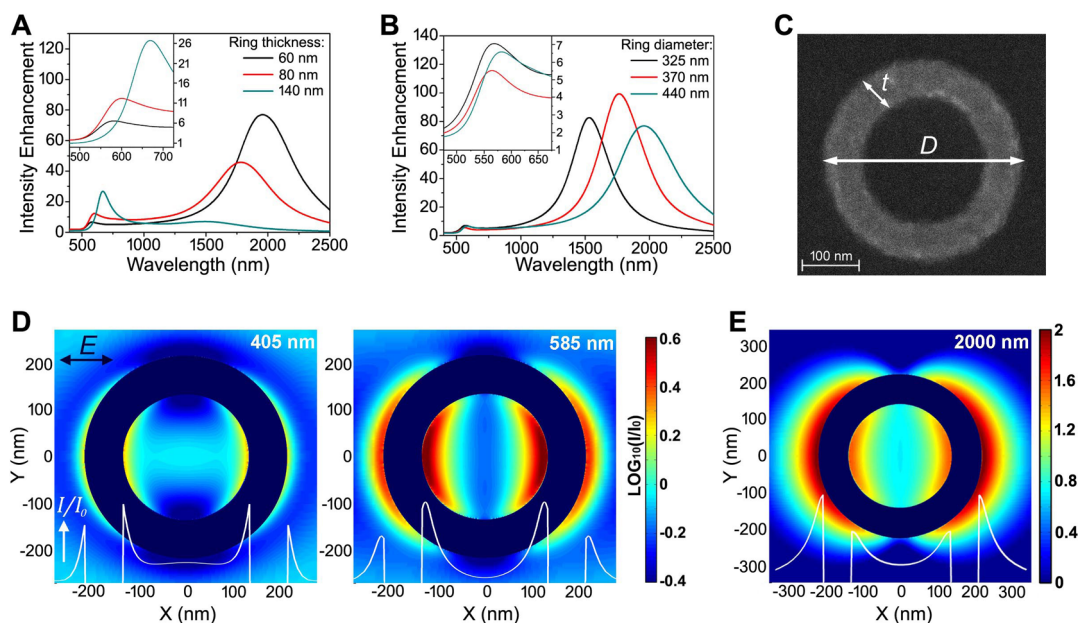
Figure 1. Electric field enhancement in PRCs. (A and B) Intensity enhancement spectra for PRCs at normal incidence, as a function of the PRC's outer diameter (A) and the PRC's thickness (B). Insets of panels A and B show same data over the visible range. The axis labels for insets are the same as those for main panels. **(C)** SEM image of a PRC with outer diameter $D = 440$ nm and thickness $t = 80$ nm (i.e., a D440t80 PRC). **(D)** Intensity enhancement for the D440t60 PRC at excitation (left) and QD emission (right) wavelengths, calculated by FDTD method and plotted in LOG scale. The white line in each map shows the value of I/I_0 through the center of the PRC. **(D)** XY intensity enhancement map for same PRC resonating at main resonance (2000 nm). For both (C) and (D), maps were calculated at a height of 10 nm above the substrate.

The overall result of the above would be a widely dissimilar and, more importantly, unpredictable performance of the fabricated devices across the chip when dimer nanoantennas are employed as plasmonic elements. Conversely, nanoantennas with larger hotspot areas would facilitate the reproducibility of the fabrication process, and also allow the exploitation of the collective behavior of the fluorophores (as opposed to near single-emitter level discussed above for dimer nanoantennas.

Metallic rings, or plasmonic ring cavities (PRCs), of 300–500 nm in diameter are a good example of such systems.[29,30] Unlike dimer and bowtie antennas, PRCs do not deliver large enhancements of electric fields in the visible region—only a small focusing of the light can be achieved with these antennas. Indeed, most of the structures used in this work offered intensity enhancement factors of less than 30 in the visible (see insets of Figure 1), while gold (Au) dimer nanoantennas resonating at similar wavelengths can achieve field enhancements one or 2 orders of magnitude larger than this.[31,32] However, and importantly, the area over which enhancement occurs is much larger in PRC structures, and so smaller field enhancements can be compensated by the larger amount of fluorophores interacting with the antenna, while providing the required predictability of the overall system.

Here, we explore this possibility to *consistently and reliably* modify the behavior of fluorophores inside Au PRC structures, with particular emphasis on the achievement of reproducible behavior across an array of similar nanostructures. We employ colloidal semiconductor QDs (CdSe/ZnS) as target entities as they have many advantages over standard fluorescent dyes. In particular, QDs photobleach less and are brighter than most standard fluorescent dyes.[33−36] Also, in contrast to strong and complicated structure–function relationships of organic dyes, modification of QDs surface chemistry can be achieved without large changes in their fluorescence behavior.[37−39] For these reasons, among others, they have been suggested as the active elements in many emitter-based systems.[37,40−50]

RESULTS AND DISCUSSION

Resonance Behavior of Plasmonic Ring Cavities. First, we used the finite difference method to calculate the resonant behavior of PRCs at normal incidence. All theoretical results shown in this work have been obtained with the use of finite-difference time-domain (FDTD) software (Lumerical) using optical data of Palik's reference book.[51] The FDTD numerical method is broadly established in computational electromagnetism to calculate the optical response of different nanostructures.[52] Figure 2A shows a typical set of cross sections obtained from calculations for a 40 nm high gold (Au) PRC on a quartz substrate, with 1 nm chromium (Cr) adhesion layer and at normal incidence. As it can be seen from this figure, a typical PRC exhibits two bright resonances. The main (dipolar) resonance (see 002.mpg) occurs in the IR, and its spectral position is highly sensitive to both the outer diameter (D) and the thickness (t) of the ring (see Figure 1C for definitions of these), with an increase in
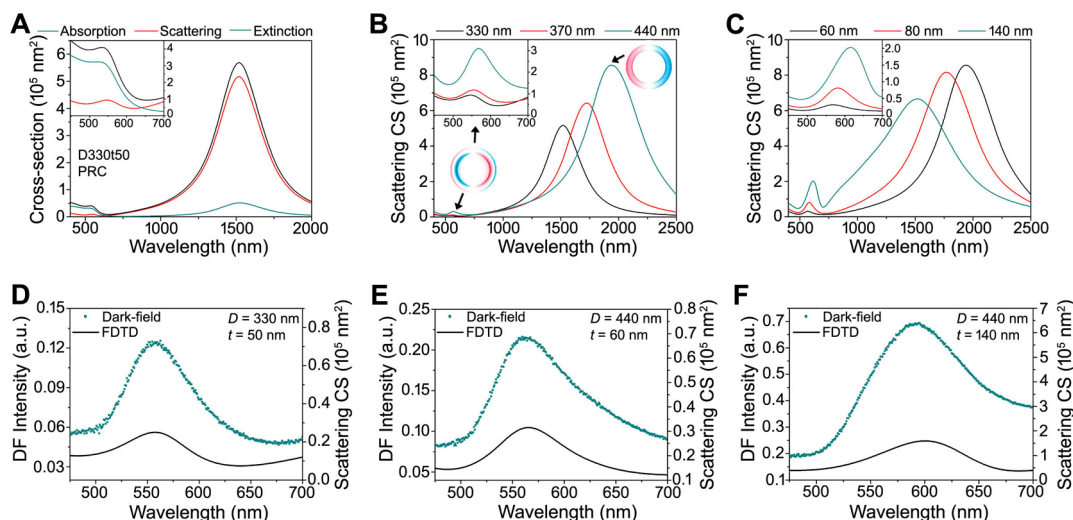
Figure 2. Resonance behavior of PRCs. (A) Example of a typical set of cross sections of a plasmonic ring cavity, calculated by the FDTD method. Panels B and C show scattering cross sections for PRCs of increasing outer diameter and increasing thickness, respectively. Each PRC has two resonant modes at normal incidence—the main dipolar resonance occurs in the near-infrared, and the higher-order resonance typically falls in the visible, below 600 nm. The axis labels for insets in panels A−C are same as those for main panels. Panels D−F compare scattering measured by dark-field (green scatter points) and cross-sections calculated by the FDTD method (solid black curve) for the higher-order mode of 3 different PRC structures. The dimensions of PRCs are indicated in the top right corner of each panel.

D leading to shift to lower energies (Figure 2B) and the opposite trend for t (Figure 2C). The second (higher-order quadrupolar) resonance occurs in the visible range, and its position is much less dependent on PRC dimensions (insets of Figures 2B and 2C). In fact, when the outer diameter of the PRC is increased by more than 100 nm (from 325 to 440 nm), this resonance red-shifts by only 20 nm. Increasing the thickness of the PRC shifts this high-order resonance to lower energies. This can be understood by considering the oscillations of charges that cause this resonance—in this case, opposite charges oscillate from the inner and to the outer edge of the ring (see charge map in Figure 2B and animation file (see 003.mpg)), and so, they are determined by its thickness.
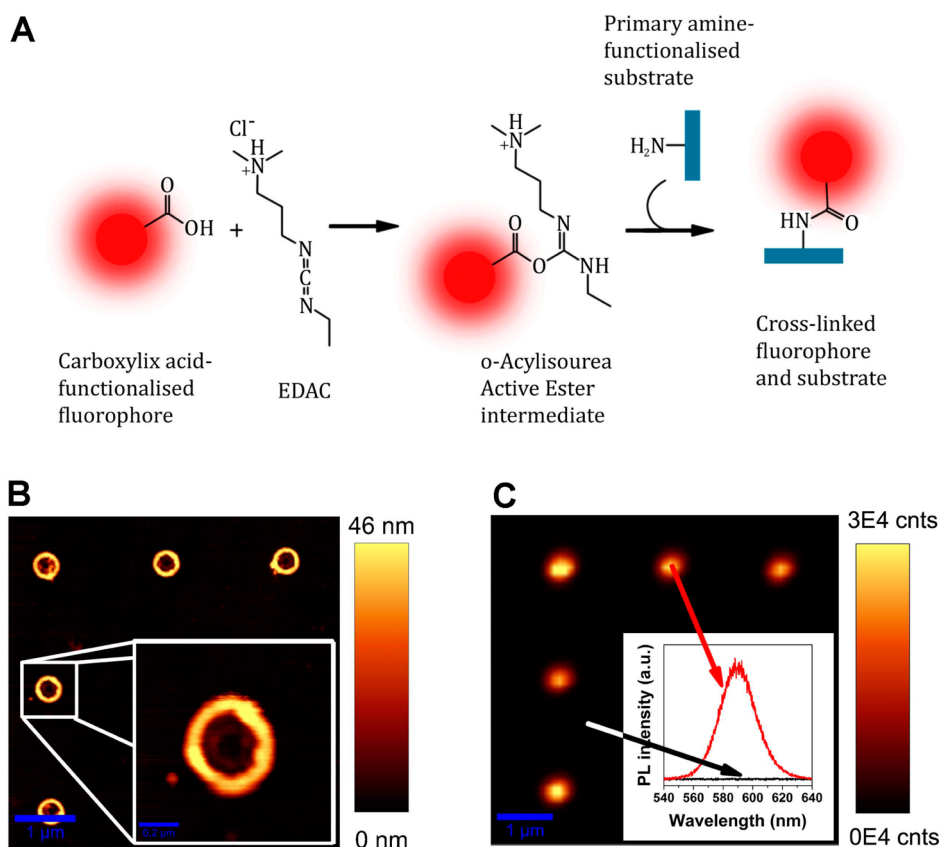
When considering this higher-order resonance, it should be noted that the absorption contribution to the total extinction by a PRC can be quite large when compared to the scattering contribution (see inset of Figure 2A). This is a typical observation for small structures[53,54] and is a further indication that the PRC's thickness is the deterministic factor for its resonance behavior at these higher frequencies. The high absorption contribution is also responsible for the aforementioned low electric field-enhancement, as it leads to damping of radiative processes and increased nonradiative losses.[55]

PRC structures fabricated in this work had the same dimensions as those indicated in Figure 1, panels A and B; SEM images of these structures and a summary of their dimensions can be found in the Supporting Information. Dark-field measurements performed on the fabricated PRCs have confirmed the position of the higher-order resonance to be within a narrow 50 nm range centered at ~580 nm (see panels D−F in Figure 2

for examples), which agreed well with predicted dark-field spectra calculated numerically (details in the Supporting Information). For this reason, QDs emitting at 585 nm were chosen as the target fluorophores to be coupled to all fabricated PRCs, allowing for various degrees of coupling of QDs' fluorescence to PRCs. Furthermore, the FDTD calculations show that for this higher-order resonance, the majority of field enhancement occurs inside the PRCs, as can be seen in Figure 1D for a PRC of 440 nm outer diameter and 80 nm thickness, from here on referred to as D440t80 PRC (see Supporting Information for other PRCs). This is in contrast to the main resonance, where the opposite is true (Figure 1E). Consequently, QDs were selectively placed inside the PRCs, at varying and predefined distances from their inner wall.

The attachment of QDs in predefined locations inside PRCs was achieved using a variation of the 2-step electron beam lithography (EBL) method reported previously.[17] Briefly, (3-aminopropyl)triethoxysilane (APTES) molecules were self-assembled on quartz in the lithographically defined ring-shaped gaps of a poly(methyl methacrylate) (PMMA) mask (see Supporting Information, Figure S1). This was then reacted with carboxylic acid (COOH)-functionalized QDs via 1-ethyl-3-(-3-(dimethyl-amino)propyl) carbodiimide (EDAC)-mediated conjugation[56] (Figure 3A). Finally, the PMMA mask was lifted off in acetone over a 24 h period.

Conjugation of QDs to quartz was confirmed by mapping their photoluminescence (PL) intensity across the array. In places where QDs attached, a characteristic Gaussian-like PL signal was observed (Figure 3C). As expected, such locations were found to be arranged in an array of 2 μm pitch, as determined by

A

Carboxylix acid-
functionalised
fluorophore

EDAC

o-Acylisourea
Active Ester
intermediate

Primary amine-
functionalised
substrate

Cross-linked
fluorophore
and substrate

B

46 nm

0 nm

1 μm

0.2 μm

C

3E4 cnts

0E4 cnts

1 μm

PL intensity (a.u.)

540 560 580 600 620 640
Wavelength (nm)

Figure 3. Attachment of quantum dots and confirmation of their localization. (A) Graphical representation of the EDAC-mediated conjugation of COOH-functionalized QDs to amine-functionalized quartz substrate. This reaction was performed inside the gaps of a PMMA mask, which was later lifted-off. Panels B and C show, respectively, an AFM image and a PL map of the PRC array with QDs attached inside the PRCs. In panel B, a ring of QDs is clearly visible inside the PRC, while in panel C the spectrum associated with one of the bright areas had a typical profile for QD emission.

the second lithographic step (Figure 3C). Further characterization was performed using noncontact atomic force microscopy (AFM), which confirmed the localization of QDs inside a PRC in a ring-like pattern (Figure 3B).

It should be noted that, due to the finite size of the e-beam (~30 nm diameter), and the subsequent prolonged ashing (needed for uniform APTES monolayers), the EBL-defined ring-shaped gaps in the PMMA mask of less than 60 nm in radius resulted in a disk-like gap instead. This led to the attachment of QDs over a circular region at the center of PRCs, rather than a ring-shaped region. This is shown diagrammatically at the top of Figure 4 for increasing radius of the gap developed in the second lithographic step (R_{QD}): the first two QD-PRC structures have disk-shaped areas of QDs (shown in red) inside a Au PRC (orange ring); but, as R_{QD} was increased, this developed into a ring-shaped area of QDs. In this way, we were able to vary the distance between the QDs and the inner wall of the PRC and thus modify the degree of coupling between the two.

Radiative Behavior of QDs Placed at Different Positions inside a Single PRC. QD-PRC separation distance was varied as described in the previous section/paragraph. The initial

characterization of the radiative properties of QDs, when coupled to Au PRC, was achieved using fluorescence lifetime imaging microscopy (FLIM). Figure 4 shows the result of this characterization for a PRC with $D \approx 440$ nm and $t \approx 60$ nm (D440t60 PRC), for 5 different radii of QD rings (R_{QD}) placed inside the PRC structure (shown graphically on top of the FLIM image). From the FLIM image, it is clear that the radiative behavior of QDs is modified significantly by the presence of PRC, and this modification increases with decreasing QD-PRC separation: the QDs' average lifetime decreases from ~6 ns for QDs placed at the center of the PRC, to ~1.5 ns for QDs in close proximity to the inner wall of the PRC. The decay rate of an emitter located in the surrounding of the PRC is modified due to two competitive processes: transfer of the energy from the emitter to the nanoparticle[57] (observed exclusively for lossy nanoparticles) and the coupling of the field originated by the emitter to the outgoing radiation.[58] The resulting modification of the emitter's decay rate, known as the Purcell effect,[59,60] has been extensively studied and applied to designing efficient nanoantennas for different applications such as, single photon emission,[61] enhancement of the fluorescence intensity,[62,63] and emission directivity.[17] In our case,
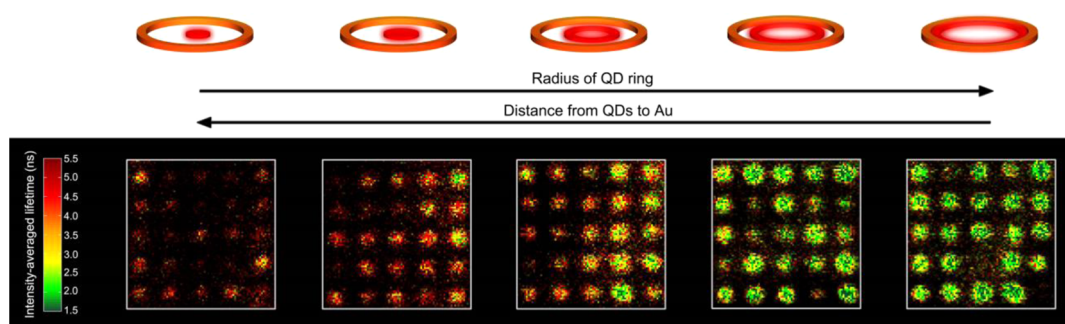
Figure 4. Fluorescence lifetime imaging microscopy of QDs inside PRCs. Main panel shows FLIM images for 5 × 5 arrays of PRCs, with rings of QDs inside, at different distances from the inner wall of the PRC. The radii of the QD rings (R_{QD}) from left to right are 15, 49, 83, 116, and 150 nm. An approximate representation of the geometry is shown graphically above each FLIM image. All PRCs were ~440 nm in diameter and had a thickness of ~60 nm.
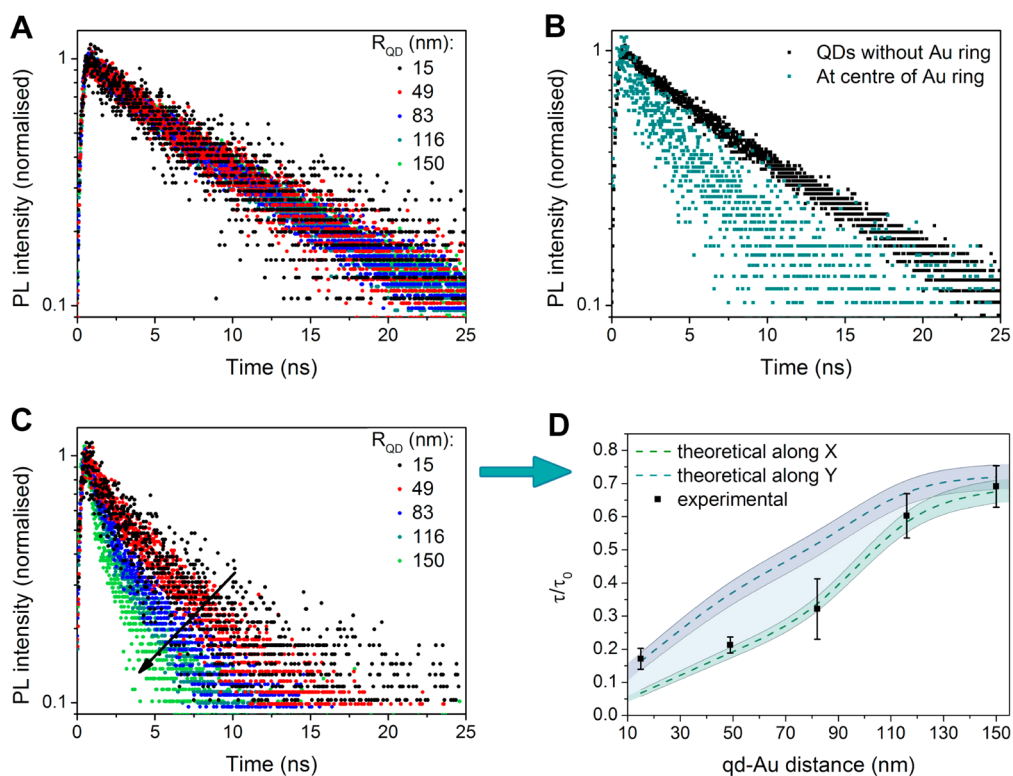

Figure 5. Radiative properties of QDs coupled to PRCs as a function of QD-PRC separation. (A) Radiative behavior of standalone rings of QDs of increasing radii (R_{QD}). (B) Radiative behavior of a small circle of QDs ($R_{QD} \approx 30$ nm) without (black scatter points) and with (green) a PRC around it. (C) Fluorescence decay behavior of rings of QDs inside a D440t60 PRC as a function of R_{QD}. The scatter points in panel D show the average lifetime values extracted from curves in panel C through biexponential fitting, normalized to the lifetime of QDs in the absence of PRCs (from panel A). Also shown in panel D are theoretical lifetime values, calculated by considering coupling of a dipole placed at various locations inside a PRC, and emitting at the QDs' emission wavelengths. The light green band is for dipoles placed along the direction of the polarization of incident light (denoted X); and light blue-gray band shows results for dipoles placed along a direction perpendicular to it (Y). The corresponding dashed lines show the values averaged over the possible locations of QDs and also over the spectral width of QDs fluorescence.

the presence of a PRC in the vicinity of QDs appreciably enhances the decay of their fluorescence (Figure 5B), and this enhancement increases as QDs are brought closer to the inner wall of the PRC (Figure 5C). Significantly, it is possible to predict the changes in the QDs' radiative behavior due to coupling to PRC theoretically by considering a dipole emitting at the QDs' emission wavelength, placed at various locations in the *XY* plane inside a PRC, and

then averaging the results over positional and spectral spreads.

To this end, we place an electric dipolar emitter, which models the dipolar transition moment of the quantum dot, with an intrinsic decay rate γ_0, in the geometric center of the plasmonic structure and calculate both the power radiated by the system and the dissipation of the energy originated by the emitter into Ohmic losses. These quantities, when normalized

to the power emitted in the absence of the antenna, yielded the enhancement of the emitter's radiative decay rate γ_R/γ_0 and of the nonradiative processes γ_{NR}/γ_0. These values were then averaged over the possible locations of QDs and over the spectral range of QDs' emission (full details of the procedure can be found in Supporting Information). From these, it is possible to calculate the theoretical change in the experimental lifetime (τ) of QDs when coupled to PRCs, relative to their original lifetime (τ_0): $\tau/\tau_0 = (\gamma_T/\gamma_0)^{-1} = \gamma_0/(\gamma_R+\gamma_{NR})$.

Figure 5D shows the spectral dependence of the reduction of experimental lifetime or, equivalently, the total decay rate enhancement for the electric dipolar emitter placed at different locations. The dashed lines in panel D of this figure show the results of the averaging procedure for QDs placed along the X and Y directions (dark blue and green, respectively), while the shaded bands of the same colors show the range of values that are acceptable theoretically. Scatter points are the experimentally obtained values of QDs' lifetime decrease.

Overall, excellent agreement was obtained between experiment and theory. Experimental values agree best with the theoretical values along X direction for large QD-PRC separation distances; at short separations, they tend toward those predicted for the Y direction. This can be explained by the fact that incident excitation was polarized along the X direction, and so QDs placed along this line couple stronger to the PRC (predicted theoretically). Hence, for very short QD-PRC distances, emission of QDs in the X-direction is quenched stronger, resulting in a proportionally smaller contribution from these QDs.

Another important aspect is the increased signal from PRC-QD structures as the separation between the ring of QDs and the inner wall of the D440t60 PRC was decreased. This can be clearly seen in the FLIM image of Figure 4. Several factors contribute to this increase. The first is the increased number of QDs deposited through the mask for increasing R_{QD}. The increase in intensity due to an increased number of QDs is expected to be linear, which was confirmed for standalone rings of QDs of various diameters (data labeled "without PRC" in Figure 6). On the other hand, the trend for QDs coupled to PRCs in this figure ("with PRC" in Figure 6) clearly has a nonlinear dependence on the number of QDs. Furthermore, increased emission intensity was observed for this case when compared to standalone QD rings, especially for the smallest QD-PRC separations. This additional increase in QD brightness is due to the Purcell effect and the increased electric field at excitation wavelength, although both are counteracted by the quenching of QDs' fluorescence due to close proximity to a metallic surface. As a result of the quenching and the low electric field enhancement in PRC structures, maximum brightness enhancement of only 50% was obtained. However, the
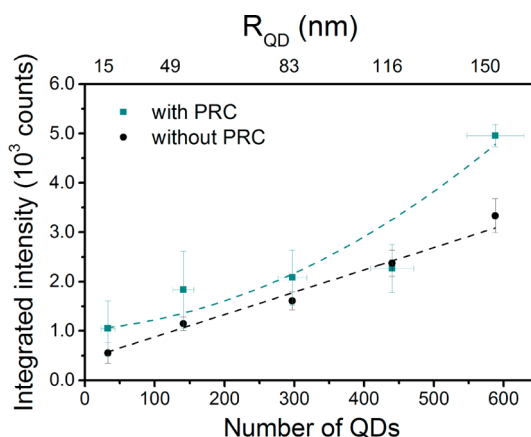

Figure 6. Integrated intensity of the rings of QD650 of various diameters, standalone (black scatter points) and coupled to a D440t60 PRC (green scatter points). The radius of the QD ring (R_{QD}) and the corresponding approximate number of QDs are indicated on the top and the bottom axis, respectively. The standalone data follows a linear relationship (dashed black line). The green dashed line for coupled QDs is a visual guide only. In both cases, emission intensity was integrated over the entire time window of lifetime measurements (100 ns).

large number of QDs yielded high emission intensities and this greatly facilitated the measurements.

QDs' Radiative Properties as a Function of PRC Dimensions. As observed above for D440t60 PRC, a large and appreciative change in the radiative behavior of QDs can be obtained even for large QD-PRC separations (Figure 5D). Thus, if the goal is to control the radiative behavior of fluorophores, it is not necessary to vary the location of the QDs inside the PRCs. QDs' radiative properties placed at the center of the rings can be controlled by varying the dimensions of the PRC instead (i.e., their outer diameter and thickness). For example, if the thickness of the PRC is kept constant while its outer diameter is increased, the rate of decay of QDs' fluorescence decreases (Figure 7A,C). On the other hand, keeping the diameter of the PRC constant, while increasing the ring's thickness, has the opposite effect (Figure 7B,D). Both of these tendencies can be explained by considering the coupling strength dependence on the PRC-QD separation distance and on the spectral overlap of the plasmonic band of the PRC and the emission band of the QDs. PRCs with larger t yield smaller QD-PRC separation distances and improved spectral overlaps with the fluorescence of QDs at 585 nm. However, it should be noted that thicker rings have negligible field enhancements at the center of PCRs for both the excitation and the emission wavelengths (Supporting Information, Figure S2), and so PRCs with thinner walls are preferable for applications where enhancement of the brightness is also desirable.

Extension to Nonconcentric Ring-Disk Systems. The results above validate PRCs for the development of plasmonics-based systems with reproducible and predictable
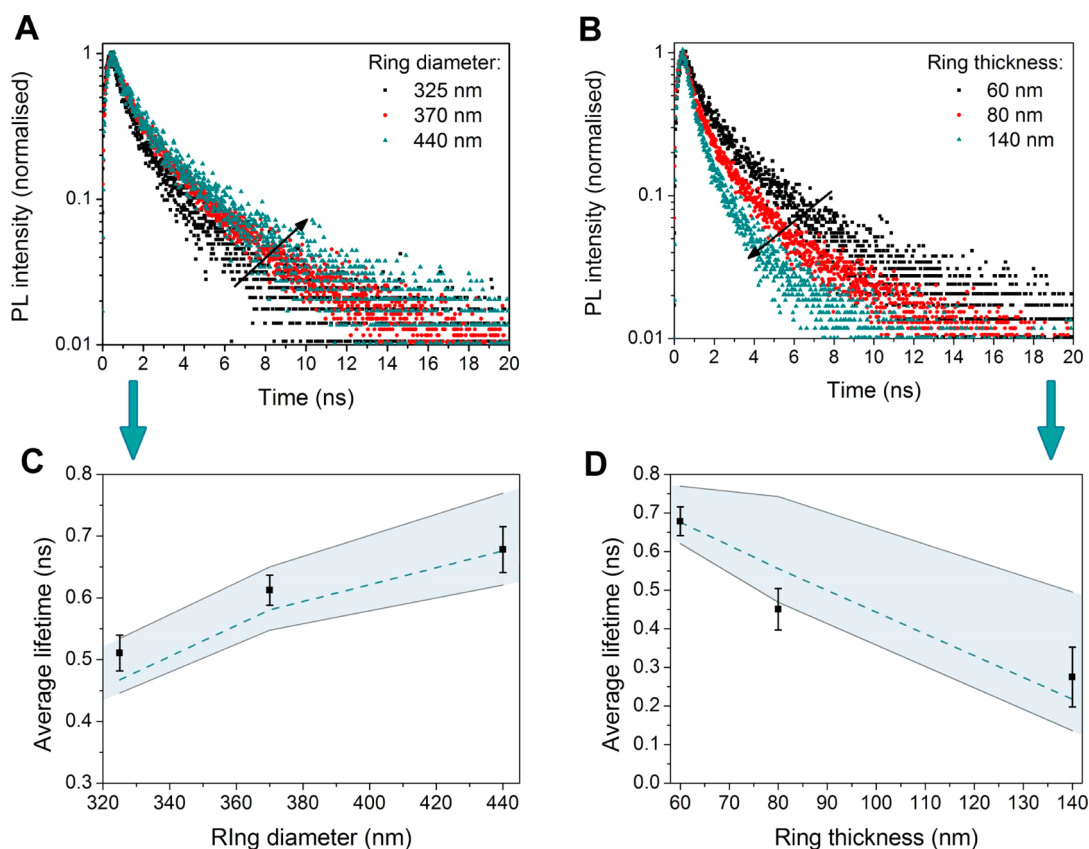
Figure 7. Radiative properties of QDs as a function of PRCs' dimensions. Panels A and C show effect of increasing PRC's outer diameter on the fluorescence decay of QDs coupled to the PRC, while panels B and D show similar data for increasing thickness of the PRC: (A,B) experimental fluorescence decay curves; (C,D) average fluorescence lifetime values extracted from the experimental data (black scatter points), and the possible theoretical values of lifetimes (light blue bands) averaged over possible locations of QDs and the spread of their emission (dashed lines).

behavior. However, the small electric field enhancement they offer, and the narrow wavelength range where their higher-order resonance occurs, limits their usefulness for emitters above 600 nm or for applications where enhancement in brightness is also essential. In the following, we show that both of these limitations can be overcome through the extension of the system to include a small disk placed close to the inner wall of the PRC. In this geometry, the disk and the PRC form a nonconcentric ring/disk cavity (NCRDC), and the dipolar mode of the disk can couple to the higher-order multipolar modes of the ring,[64−67] the latter occurring over a wide spectral region in the visible. The coupling allows the otherwise dark multipolar modes of the ring to become dipole-active, facilitating the propagation of these modes to the far field.[64,68] Figure 8 demonstrates this for disks of various diameters placed inside a PRC of 350 nm outer diameter and 45 nm thickness (D350t45). The intensity enhancement profile at 650 nm (bottom panel of Figure 8A) clearly shows the disk resonating in dipolar fashion; on the other hand, several intensity enhancement "lobes" can be seen around the ring, which is indicative of the multipolar behavior (see 004.mpg).

Figure 8B shows the experimental dark-field data (top panel) and numerically calculated far-field scattering

(bottom panel) for a D350t45 PRC coupled to disks of different diameters, ranging from ∼30 to 90 nm, placed 20 nm inside and away from the PRC. Unmistakably, the size of the disk determines the position and strength of its dipolar resonance and, consequently, the position and strength of the coupled modes of the NCRDC. These coupled modes are then able to propagate to the far-field, resulting in increased dark-field signal at visible wavelengths. In fact, we show that ∼30-fold increase in the measured DF intensity can be obtained for these NCRDCs.

Figure 8C shows similar data for the largest disk (d = 90 nm) placed at increasing distances from the inner wall of the D350t45 PRC. The strength of the coupling notably decreases as the distance between the two components is increased, indicated by the reduced strength of some of the NCRDC resonances, particularly the lower energy ones. Several resonances can be clearly seen in the theoretical scattering data, marked i through iv in the bottom panel of Figure 8C. Each of these resonances can be attributed to coupling to a different multipolar resonance of the ring (see charge maps (see 005.mpg) i−iv in Figure 8D). Importantly, the results in Figure 8C promise improved far-field propagation of radiation, even for disk-PRC
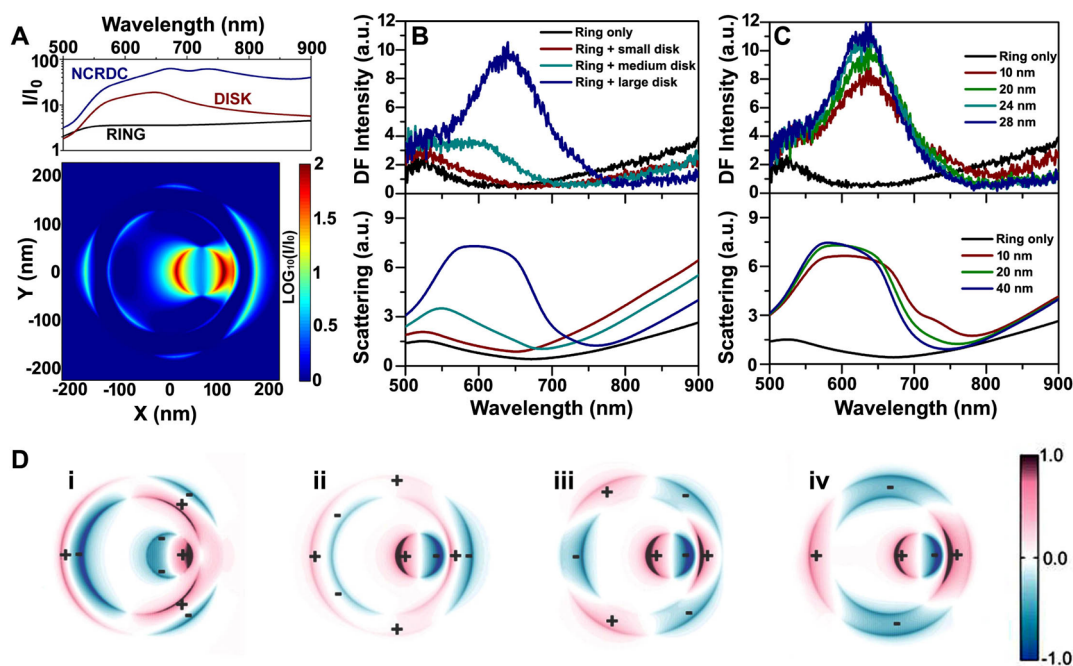
Figure 8. Optical response of nonconcentric ring-disk cavities. (a) Intensity enhancement by a NCRDC consisting of a D350t45 PRC and a disk of 90 nm diameter placed at a distance of 20 nm away from the inner wall of the PRC. The top panel compares the spectral response of the NCRDC at that of its constituent components and the bottom panel shows an intensity enhancement map for this structure at 650 nm excitation. Panels B and C compare the experimental (top panels) and theoretical (bottom panels) scattering from the NCRDC consisting of D350t45 PRC and (B) disks of various diameter (30, 60 and 90 nm); (C) a disk of 90 nm diameter, placed at increasing distances from the inner wall of the PRC. Panel D shows charge distributions for several resonances of NCRDC, the spectral positions of which are indicated by i–iv in panel C.

gaps larger than 30 nm. This is a great advantage, as large gaps facilitate device fabrication and also allow for reduced quenching effects due to proximity of fluorophores to metallic surfaces.

As can be seen from Figure 8B,C, experimental scattering of radiation showed some deviation from theoretical calculations. In particular, resonances were less pronounced and in all cases the dominant peak occurred at 650 nm. This was due to a combination of imperfections in the disks and PRC geometries, together with the resulting nonuniform gap between them (discussion of these and their effect can be found in the Supporting Information).

Another potential advantage of the NCRDC geometry is the increased field enhancement in the gap between the disk and the ring, at wavelengths larger than the position of the dipolar resonance of the disk. Figure 8A compares the theoretical near-field enhancement in the middle of the gap of the D350t45 PRC coupled to 90 nm disk placed 20 nm away, to enhancements that can be obtained 10 nm away from each of the constituent structures. At 650 nm, the intensity in the gap of the NCRDC was found to be 5 times larger than for just a disk and, more interestingly, 30 times larger than for the PRC. This agrees well with the 30-fold increase in scattering intensity observed experimentally for this NCRDC. Crucially, most of the enhancement is achieved in the visible range (Figure 8A), suggesting that the detrimental high field

intensities at excitation wavelengths can be avoided. Finally, and importantly, in this configuration the active region of the NCRDC (the hotspot) is still reasonably large when compared to hotspots of dimer nanoantennas; in fact, even for small gaps between components, we approximate the area of the active region to be almost 3 times larger in area than for a dimer disk antenna resonating at the same wavelength (see Supporting Information).

CONCLUSIONS

Plasmonics-based emitting devices hold great potential as photonic components for on-chip optical data processing applications. However, the choice of the geometry of the plasmonic structure in such devices is limited by the properties of the fluorophore used. When colloidal QDs are utilized as the active elements within a plasmonics-based device, several of their properties must be taken into account, including their behavior at single QD level, their photostability at high electric field intensities, the quenching of their emission when in immediate proximity to metallic surfaces and the distribution of their sizes within a typical sample. As a consequence of these, it becomes clear that dimer antennas should be avoided when combined with colloidal QDs, as such a combination would result in a very unpredictable and unreliable system. However, many of the aforementioned limitations can be overcome by employing antenna

geometries with larger hotspot areas instead, although at the price of reduced electric field enhancements. In this work, we showed that PRCs satisfy this criteria, and that they can be used to consistently and *deterministically* alter the radiative behavior of QDs placed in their vicinity.

In particular, the radiative decay of fluorescence of QDs placed at the center of PRCs was found to depend greatly on the dimensions of the plasmonic nanostructure, with opposite trends observed for changes in the PRC's outer diameter and their thicknesses. Additionally, the rate of fluorescence decay can be further enhanced by reducing the distance between QDs and the inner wall of the PRC, through precise fabrication methods. In both cases, excellent agreement was achieved between experimental and theoretical data,

attesting to the reliability of the performance of this system.

For QDs coupled to PRCs, only a small increase in QDs' brightness was observed (up to 50%), limited by the small electric field enhancements provided by the PRC structures. We proposed that brightness enhancement can be improved by extending this system to include a metallic disk placed off-center and inside the PRC, thus forming a nonconcentric ring-disk cavity. This plasmonic geometry significantly enhances the electric field intensities in the cavity, and also offers improved far-field propagation of re-emitted radiation. Yet, NCRDCs still have relatively large hotspots permitting exploitation of the collective behavior of QDs and reduction of detrimental consequences of colloidal QDs' properties.

EXPERIMENTAL METHODS

Sample Fabrication. Ring cavities were fabricated by using the standard electron-beam lithography method, using PMMA as a resist and by evaporating 1 nm of Cr at a rate of 0.2 Å/s and then 40 nm of gold at a rate of 2 Å/s. The second EBL layer was then exposed, with the gaps in PMMA mask aligned to specific regions of ring cavities. A self-assembled monolayer of amino-terminated molecules was formed in these gaps and the amino-groups were reacted with carboxyl groups of the quantum dots' stabilizing shell, thereby chemically attaching QDs to the substrate.

Dark-field (DF) Measurements. Samples were illuminated using a standard white light lamp. The incident light was focused onto the sample using a dark-field objective; scattered radiation was collected with the same objective and directed toward either an avalanche photodiode (APD) (for obtaining scattered intensity images) or the spectrometer (for collecting DF spectra). Spectra were collected from on and off the structures to account for the background, and corrections for the detector's spectral dependence and lamp's spectrum were performed by collecting reference spectra from a reflectance standard.

FLIM and Lifetime Measurements. QDs were excited with a pulsed laser (405 or 488 nm) from below. Emission was collected from the top with an optical fiber of 50 μm diameter, passed through band-pass filters, and directed toward an APD. To obtain photoluminescence (PL) decay curves, the intensity of emission was recorded as a function of time. FLIM images were obtained by recording decay curves at each pixel of an image. Fluorescence decays curves were fitted with biexponential functions ($I = I_{BGR} + \sum_i \exp(\alpha_i \tau_i/t)$) where τ_i and α_i are the lifetimes and their corresponding relative weights. The averaged fluorescence lifetime was then determined in the standard manner ($\bar{\tau} = \sum_i(\alpha_i\tau_i^2)/\sum_i(\alpha_i\tau_i)$).

Confirmation of QD Conjugation. PL mapping of arrays was achieved by collecting spectra from QDs' excited by 532 nm laser, as the sample was scanned. AFM imaging was performed in noncontact mode at low speeds. Both measurements were performed on WITec Alpha 300 RS.

Numerical Calculations. Numerical solution of the near and far field response for the systems treated in this manuscript have been obtained by solving Maxwell's equations for a plane wave incident on the exact geometry of an individual gold nanoantenna (PRC or NCRDC) on a quartz (SiO_2) substrate, with 1 nm Cr layer underneath the structure. The substrate and the adhesion layer were always included in the model to fully consider the substrate effects on the optical properties, which have been shown to be critical in several publications.[69,70] The simulations have been performed with use of finite-difference time-domain software (Lumerical) using optical data of Palik's reference book.[51] This numerical method is broadly established in

computational electromagnetism to calculate the optical response of different nanostructures.[52] It consists of a direct implementation of the Maxwell time-dependent curl equations to solve the temporal variations of electromagnetic waves within a finite space that contains objects of arbitrary shape and properties (perfectly matched layers were used as boundary conditions). In practice, the space including the scatterer is discretized into a grid that contains the basic element of this discretization, the Yee cell. The precision of the results depends both on the number of the cells used in the simulation and the appropriate selection of the simulation time. The presented results are fully converged, thus they can be considered an exact solution of Maxwell's equations. Additionally, some of the results shown have been tested with other solving methods (FEM (using COMSOL multiphysics) and the discrete dipole approximation (DDA)[71], producing very good agreement.

Additional details of the experimental methods can be found in the Supporting Information.

Conflict of Interest: The authors declare no competing financial interest.

Supporting Information Available: Fabrication procedures; QDs optical properties; details of theoretical calculations of dark field spectra; averaging of theoretical decay rates for comparison with experimental lifetime data; effect of deviations from perfect geometries on dark-field spectra of NCRDCs, charge distribution calculations; comparison of hotspots of NCRDC and disk-dimer nanoantenna; SEM images and dimensions of nanoantennas; intensity enhancement maps for all PRCs; non-normalized lifetime data for Figure 5; separate movie files of oscillating charges for different resonances of PRCs and NCRDCs. This material is available free of charge *via* the Internet at http://pubs.acs.org.

REFERENCES AND NOTES

1. Giannini, V.; Fern, A. I.; Heck, S. C.; Maier, S. A. Plasmonic Nanoantennas: Fundamentals and Their Use in Controlling the Radiative Properties of Nanoemitters. *Chem. Rev.* **2011**, *111*, 3888–3912.
2. Schuller, J. a; Barnard, E. S.; Cai, W.; Jun, Y. C.; White, J. S.; Brongersma, M. L. Plasmonics for Extreme Light Concentration and Manipulation. *Nat. Mater.* **2010**, *9*, 193–204.

3. Stockman, M. I. Nanoplasmonics: Past, Present, and Glimpse into Future. *Opt. Express* **2011**, *19*, 22029–22106.

4. Xie, J.; Zhang, Q.; Lee, J. Y.; Wang, D. I. C. The Synthesis of SERS-Active Gold Nanoflower Tags for *in Vivo* Applications. *ACS Nano* **2008**, *2*, 2473–2480.

5. Giannini, V.; Rodríguez-Oliveros, R.; Sánchez-Gil, J. a. Surface Plasmon Resonances of Metallic Nanostars/Nanoflowers for Surface-Enhanced Raman Scattering. *Plasmonics* **2010**, *5*, 99–104.

6. Wang, X.; Li, M.; Meng, L.; Lin, K.; Feng, J.; Huang, T.; Yang, Z.; Ren, B. Probing the Location of Hot Spots by Surface-Enhanced Raman Spectroscopy: Toward Uniform Substrates. *ACS Nano* **2014**, *8*, 528–536.

7. Karabeber, H.; Huang, R.; Iacono, P.; Samii, J. M.; Pitter, K.; Holland, E. C.; Kircher, M. F. Guiding Brain Tumor Resection Using Surface-Enhanced Raman Scattering Nanoparticles and a Hand-Held Raman Scanner. *ACS Nano* **2014**, 9755–9766.

8. Tian, Z.-Q.; Ren, B.; Wu, D.-Y. Surface-Enhanced Raman Scattering: From Noble to Transition Metals and from Rough Surfaces to Ordered Nanostructures. *J. Phys. Chem. B* **2002**, *106*, 9463–9483.

9. Tian, Z. Q. Surface-Enhanced Raman Spectroscopy: Advancements and Applications. *J. Raman Spectrosc.* **2005**, *36*, 466–470.

10. Pucci, a.; Neubrech, F.; Weber, D.; Hong, S.; Toury, T.; de la Chapelle, M. L. Surface Enhanced Infrared Spectroscopy Using Gold Nanoantennas. *Phys. Status Solidi* **2010**, *247*, 2071–2074.

11. D'Andrea, C.; Toma, A.; Huck, C.; Neubrech, F.; Messina, E.; Fabrizio, E.; Di Lamy, M.; Chapelle, D.; La Gucciardi, P. G.; Fazio, B.; *et al.* Optical Nanoantennas for Multiband Surface-Enhanced Infrared and Raman Spectroscopy. *ACS Nano* **2013**, *7*, 3522–3531.

12. Zhang, J.; Zhao, J.; He, H.; Zhang, H.; Li, H. Studies on the Surface-Enhanced Infrared Spectroscopy of Langmuir–Blodgett Monolayers of Azobenzene Carboxylic Acid on Silver Island Films. *Langmuir* **1998**, *14*, 5521–5525.

13. Ataka, K.; Yotsuyanagi, T.; Osawa, M. Potential-Dependent Reorientation of Water Molecules at an Electrode/Electrolyte Interface Studied by Surface-Enhanced Infrared Absorption Spectroscopy. *J. Phys. Chem.* **1996**, *100*, 10664–10672.

14. Alonso-González, P.; Albella, P.; Golmar, F.; Arzubiaga, L.; Casanova, F.; Hueso, L. E.; Aizpurua, J.; Hillenbrand, R. Visualizing the Near-Field Coupling and Interference of Bonding and Anti-bonding Modes in Infrared Dimer Nanoantennas. *Opt. Express* **2013**, *21*, 1270–1280.

15. Kawata, S.; Inouye, Y.; Verma, P. Plasmonics for Near-Field Nano-imaging and Superlensing. *Nat. Photonics* **2009**, *3*, 388–394.

16. Schnell, M.; Garcia-Etxarri, A. Amplitude-and Phase-Resolved Near-Field Mapping of Infrared Antenna Modes by Transmission-Mode Scattering-Type Near-Field Microscopy. *J. Phys. Chem. C* **2010**, *114*, 7341–7345.

17. Curto, A. G.; Volpe, G.; Taminiau, T. H.; Kreuzer, M. P.; Quidant, R.; van Hulst, N. F. Unidirectional Emission of a Quantum Dot Coupled to a Nanoantenna. *Science* **2010**, *329*, 930–933.

18. Ureña, E. B.; Kreuzer, M. P.; Itzhakov, S.; Rigneault, H.; Quidant, R.; Oron, D.; Wenger, J. Excitation Enhancement of a Quantum Dot Coupled to a Plasmonic Antenna. *Adv. Mater.* **2012**, *24*, OP314–OP320.

19. Curto, A. G.; Taminiau, T. H.; Volpe, G.; Kreuzer, M. P.; Quidant, R.; van Hulst, N. F. Multipolar Radiation of Quantum Emitters with Nanowire Optical Antennas. *Nat. Commun.* **2013**, *4*, 1750.

20. Galloway, C. M.; Kreuzer, M. P.; Aćimović, S. S.; Volpe, G.; Correia, M.; Petersen, S. B.; Neves-Petersen, M. T.; Quidant, R. Plasmon-Assisted Delivery of Single Nano-objects in an Optical Hot Spot. *Nano Lett.* **2013**, *13*, 4299–4304.

21. Geiselmann, M.; Marty, R.; Renger, J.; García de Abajo, F. J.; Quidant, R. Deterministic Optical-near-Field-Assisted Positioning of Nitrogen-Vacancy Centers. *Nano Lett.* **2014**, *14*, 1520–1525.

22. Patterson, G. H.; Piston, D. W. Photobleaching in Two-Photon Excitation Microscopy. *Biophys. J.* **2000**, *78*, 2159–2162.

23. Song, L.; Hennink, E. J.; Young, I. T.; Tanke, H. J. Photobleaching Kinetics of Fluorescein in Quantitative Fluorescence Microscopy. *Biophys. J.* **1995**, *68*, 2588–2600.

24. Dyumaev, K. M.; Manenkov, A. A.; Maslyukov, A. P.; Matyushin, G. A.; Nechitailo, V. S.; Prokhorov, A. M. Dyes in Modified Polymers: Problems of Photostability and Conversion Efficiency at High Intensities. *J. Opt. Soc. Am. B* **1992**, *9*, 143–151.

25. Gordon, M. P.; Ha, T.; Selvin, P. R. Single-Molecule High-Resolution Imaging with Photobleaching. *Proc. Natl. Acad. Sci. U.S.A.* **2004**, *101*, 6462–6465.

26. Shimizu, K.; Neuhauser, R. Blinking Statistics in Single Semiconductor Nanocrystal Quantum Dots. *Phys. Rev. B* **2001**, *63*, 205316.

27. Van Sark, W. G. J. H. M.; Frederix, P. L. T. M.; Bol, A. a.; Gerritsen, H. C.; Meijerink, A. Blueing, Bleaching, and Blinking of Single CdSe/ZnS Quantum Dots. *ChemPhysChem* **2002**, *3*, 871–879.

28. Nirmal, M.; Brus, L. Luminescence Photophysics in Semiconductor Nanocrystals. *Acc. Chem. Res.* **1999**, *32*, 407–414.

29. Aizpurua, J.; Hanarp, P.; Sutherland, D.; Käll, M.; Bryant, G.; García de Abajo, F. Optical Properties of Gold Nanorings. *Phys. Rev. Lett.* **2003**, *90*, 057401.

30. Nordlander, P. The Ring: A Leitmotif in Plasmonics. *ACS Nano* **2009**, *3*, 488–492.

31. Kinkhabwala, A.; Yu, Z.; Fan, S.; Avlasevich, Y.; Müllen, K.; Moerner, W. E. Large Single-Molecule Fluorescence Enhancements Produced by a Bowtie Nanoantenna. *Nat. Photonics* **2009**, *3*, 654–657.

32. Rosen, D. a; Tao, A. R. Modeling the Optical Properties of Bowtie Antenna Generated by Self-Assembled Ag Triangular Nanoprisms. *ACS Appl. Mater. Interfaces* **2014**, *6*, 4134–4142.

33. Bradburne, C. E.; Delehanty, J. B.; Boeneman Gemmill, K.; Mei, B. C.; Mattoussi, H.; Susumu, K.; Blanco-Canosa, J. B.; Dawson, P. E.; Medintz, I. L. Cytotoxicity of Quantum Dots Used for *in Vitro* Cellular Labeling: Role of QD Surface Ligand, Delivery Modality, Cell Type, and Direct Comparison to Organic Fluorophores. *Bioconjugate Chem.* **2013**, *24*, 1570–1583.

34. Resch-Genger, U.; Grabolle, M.; Cavaliere-Jaricot, S.; Nitschke, R.; Nann, T. Quantum Dots *versus* Organic Dyes as Fluorescent Labels. *Nat. Methods* **2008**, *5*, 763–775.

35. Hod, I.; González-Pedro, V.; Tachan, Z.; Fabregat-Santiago, F.; Mora-Seró, I.; Bisquert, J.; Zaban, A. Dye *versus* Quantum Dots in Sensitized Solar Cells: Participation of Quantum Dot Absorber in the Recombination Process. *J. Phys. Chem. Lett.* **2011**, *2*, 3032–3035.

36. Montón, H.; Nogués, C.; Rossinyol, E.; Castell, O.; Roldán, M. QDs *versus* Alexa: Reality of Promising Tools for Immunocytochemistry. *J. Nanobiotechnol.* **2009**, *7*, 4.

37. Wegner, K. D.; Lanh, P. T.; Jennings, T.; Oh, E.; Jain, V.; Fairclough, S. M.; Smith, J. M.; Giovanelli, E.; Lequeux, N.; Pons, T.; *et al.* Influence of Luminescence Quantum Yield, Surface Coating, and Functionalization of Quantum Dots on the Sensitivity of Time-Resolved FRET Bioassays. *ACS Appl. Mater. Interfaces* **2013**, *5*, 2881–2892.

38. Hines, D.; Kamat, P. Quantum Dot Surface Chemistry: Ligand Effects and Electron Transfer Reactions. *J. Phys. Chem. C* **2013**, *117*, 14418–14426.

39. Cheng, X.; Lowe, S. B.; Ciampi, S.; Magenau, A.; Gaus, K.; Reece, P. J.; Gooding, J. J. Versatile "Click Chemistry" Approach to Functionalizing Silicon Quantum Dots: Applications toward Fluorescent Cellular Imaging. *Langmuir* **2014**, *30*, 5209–5216.

40. Shirasaki, Y.; Supran, G. J.; Bawendi, M. G.; Bulović, V. Emergence of Colloidal Quantum-Dot Light-Emitting Technologies. *Nat. Photonics* **2012**, *7*, 13–23.

41. Kouhnavard, M.; Ikeda, S.; Ludin, N. a.; Ahmad Khairudin, N. B.; Ghaffari, B. V.; Mat-Teridi, M. a.; Ibrahim, M. a.; Sepeai, S.; Sopian, K. A Review of Semiconductor Materials as

Sensitizers for Quantum Dot-Sensitized Solar Cells. *Renew. Sustain. Energy Rev.* **2014**, *37*, 397–407.

42. Nabiev, I.; Rakovich, A.; Sukhanova, A.; Lukashev, E.; Zagidullin, V.; Pachenko, V.; Rakovich, Y. P.; Donegan, J. F.; Rubin, A. B.; Govorov, A. O. Fluorescent Quantum Dots as Artificial Antennas for Enhanced Light Harvesting and Energy Transfer to Photosynthetic Reaction Centers. *Angew. Chem., Int. Ed. Engl.* **2010**, *49*, 7217–7221.

43. Kamat, P. Quantum Dot Solar Cells. The Next Big Thing in Photovoltaics. *J. Phys. Chem. Lett.* **2013**, *4*, 908–918.

44. Rakovich, A.; Sukhanova, A.; Bouchonville, N.; Lukashev, E.; Oleinikov, V.; Artemyev, M.; Lesnyak, V.; Gaponik, N.; Molinari, M.; Troyon, M.; *et al*. Resonance Energy Transfer Improves the Biological Function of Bacteriorhodopsin within a Hybrid Material Built from Purple Membranes and Semiconductor Quantum Dots. *Nano Lett.* **2010**, *10*, 2640–2648.

45. Díaz, S. a; Giordano, L.; Azcárate, J. C.; Jovin, T. M.; Jares-Erijman, E. a. Quantum Dots as Templates for Self-Assembly of Photoswitchable Polymers: Small, Dual-Color Nanoparticles Capable of Facile Photomodulation. *J. Am. Chem. Soc.* **2013**, *135*, 3208–3217.

46. Rakovich, A.; Nabiev, I.; Sukhanova, A.; Lesnyak, V.; Gaponik, N.; Rakovich, Y. P.; Donegan, J. F. Large Enhancement of Nonlinear Optical Response in a Hybrid Nanobiomaterial Consisting of Bacteriorhodopsin and Cadmium Telluride Quantum Dots. *ACS Nano* **2013**, *7*, 2154–2160.

47. Rakovich, A.; Donegan, J. F.; Oleinikov, V.; Molinari, M.; Sukhanova, A.; Nabiev, I.; Rakovich, Y. P. Linear and Nonlinear Optical Effects Induced by Energy Transfer from Semiconductor Nanoparticles to Photosynthetic Biological Systems. *J. Photochem. Photobiol. C Photochem. Rev.* **2014**, *20*, 17–32.

48. Petryayeva, E.; Algar, W. R.; Medintz, I. L. Quantum Dots in Bioanalysis: A Review of Applications across Various Platforms for Fluorescence Spectroscopy and Imaging. *Appl. Spectrosc.* **2013**, *67*, 215–252.

49. Rakovich, A.; Savateeva, D.; Rakovich, T.; Donegan, J. F.; Rakovich, Y. P.; Kelly, V.; Lesnyak, V.; Eychmüller, A. CdTe Quantum Dot/Dye Hybrid System as Photosensitizer for Photodynamic Therapy. *Nanoscale Res. Lett.* **2010**, *5*, 753–760.

50. Tatsiana Y, Rakovich; Mahfoud, O. K.; Mohamed, B. M.; Prina-Mello, A.; Crosbie-Staunton, K.; Broeck, T. Van Den; Kimpe, L. De; Sukhanova, A.; Baty, D.; Rakovich, A.; *et al*. Highly Sensitive Single Domain Antibody-Quantum Dot Conjugates for Detection of HER2 Biomarker in Lung and Breast Cancer Cells. *ACS Nano* **2014**, *8*, 5682–5695.

51. Edward D, Palik. *Handbook of Optical Constants of Solids*; Elsevier: The Netherlands, 1997; pp 5–114.

52. Weber, D.; Albella, P.; Alonso-González, P.; Neubrech, F.; Gui, H.; Nagao, T.; Hillenbrand, R.; Aizpurua, J.; Pucci, A. Longitudinal and Transverse Coupling in Infrared Gold Nanoantenna Arrays: Long Range *versus* Short Range Interaction Regimes. *Opt. Express* **2011**, *19*, 15047–15061.

53. Bohren, C. F.; Huffman, D. R. Extinction. In *Absorption and Scattering of Light by Small Particles*; Wiley-VCH Verlag GmbH: Weinheim, Germany, 2007; pp 286–324.

54. Jain, P. K.; Lee, K. S.; El-Sayed, I. H.; El-Sayed, M. A. Calculated Absorption and Scattering Properties of Gold Nanoparticles of Different Size, Shape, and Composition: Applications in Biological Imaging and Biomedicine. *J. Phys. Chem. B* **2006**, *110*, 7238–7248.

55. Albella, P.; Poyli, A.; Schmidt, M. K.; Maier, S. A.; Moreno, F.; JoséSaenz, J.; Aizpurua, J. Low-Loss Electric and Magnetic Field-Enhanced Spectroscopy with Subwavelength Silicon Dimers. *J. Phys. Chem. C* **2013**, *117*, 13573–13584.

56. Manfrinato, V. R.; Wanger, D. D.; Strasfeld, D. B.; Han, H.-S.; Marsili, F.; Arrieta, J. P.; Mentzel, T. S.; Bawendi, M. G.; Berggren, K. K. Controlled Placement of Colloidal Quantum Dots in Sub-15 nm Clusters. *Nanotechnology* **2013**, *24*, 125302.

57. Anger, P.; Bharadwaj, P.; Novotny, L. Enhancement and Quenching of Single-Molecule Fluorescence. *Phys. Rev. Lett.* **2006**, *96*, 113002.

58. Ruppin, R. Decay of an Excited Molecule near a Small Metal Sphere. *J. Chem. Phys.* **1982**, *76*, 1681–1684.

59. Purcell, E. M. Spontaneous Emission Probabilities at Radio Frequencies. *Phys. Rev.* **1946**, *69*, 681.

60. Koenderink, A. F. On the Use of Purcell Factors for Plasmon Antennas. *Opt. Lett.* **2010**, *35*, 4208–4210.

61. Novotny, L.; van Hulst, N. Antennas for Light. *Nat. Photonics* **2011**, *5*, 83–90.

62. Aroca, R.; Teo, G.; Mohan, H. Plasmon-Enhanced Fluorescence and Spectral Modification in SHINEF. *J. Phys. Chem. C* **2011**, *115*, 20419–20424.

63. Albella, P.; Alcaraz de la Osa, R.; Moreno, F.; Maier, S. A. Electric and Magnetic Field Enhancement with Ultralow Heat Radiation Dielectric Nanoantennas: Considerations for Surface-Enhanced Spectroscopies. *ACS Photonics* **2014**, *1*, 524–529.

64. Hao, F.; Nordlander, P.; Sonnefraud, Y.; Van Dorpe, P.; Maier, S. A. Tunability of Subradiant Dipolar and Fano-Type Plasmon Resonances in Metallic Ring/Disk Cavities: Implications for Nanoscale Optical Sensing. *ACS Nano* **2009**, *3*, 643–652.

65. Sonnefraud, Y.; Verellen, N.; Sobhani, H.; Vandenbosch, G. A. E.; Moshchalkov, V. V.; Dorpe, P.; Van Nordlander, P.; Maier, S. A. Experimental Realization of Subradiant, Superradiant, and Fano Resonances in Ring/disk Plasmonic Nanocavities. *ACS Nano* **2010**, *4*, 4–10.

66. Fu, Y.; Zhang, J.; Yu, Y.; Luk'yanchuk, B. Generating and Manipulating Higher Order Fano Resonances in Dual-Disk Ring Plasmonic Nanostructures. *ACS Nano* **2012**, *6*, 5130–5137.

67. Cetin, A. E.; Altug, H. Fano Resonant Ring/disk Plasmonic Nanocavities on Conducting Substrates for Advanced Biosensing. *ACS Nano* **2012**, *6*, 9989–9995.

68. Abb, M.; Wang, Y.; Albella, P.; de Groot, C. H.; Aizpurua, J.; Muskens, O. L. Interference, Coupling, and Nonlinear Control of High-Order Modes in Single Asymmetric Nanoantennas. *ACS Nano* **2012**, *6*, 6462–6470.

69. Albella, P.; Moreno, F.; Saiz, J. M.; González, F. Surface Inspection by Monitoring Spectral Shifts of Localized Plasmon Resonances. *Opt. Express* **2008**, *16*, 12872–12879.

70. Knight, M. W.; Wu, Y.; Lassiter, J. B.; Nordlander, P.; Halas, N. J. Substrates Matter: Influence of an Adjacent Dielectric on an Individual Plasmonic Nanoparticle. *Nano Lett.* **2009**, *9*, 2188–2192.

71. de la Osa, R. A.; Albella, P.; Saiz, J. M.; González, F.; Moreno, F. Extended Discrete Dipole Approximation and Its Application to Bianisotropic Media. *Opt. Express* **2010**, *18*, 23865–23871.